PCCP

PAPER

View Article Online
View Journal | View Issue

Cite this: *Phys. Chem. Chem. Phys.*, 2025, **27**, 12699

Dynamical insights into denitrogenation of 1-pyrazoline: exploring pathways *via* transition states and a second-order saddle†

Renuka Pradhan and Upakarasamy Lourderaj *

Received 28th February 2025,
Accepted 22nd May 2025

DOI: 10.1039/d5cp00798d

rsc.li/pccp

The mechanism of 1-pyrazoline denitrogenation has garnered significant attention due to its remarkable stereoselectivity. In this study, the thermal denitrogenation mechanism of 1-pyrazoline was investigated using *ab initio* classical trajectory simulations to elucidate post-transition state and post-second-order saddle dynamics. Trajectories initiated from the synchronous transition state region predominantly followed the minimum energy pathway, forming the trimethylene diradical intermediate, which subsequently yielded cyclopropane with a preference for single inversion of the configuration. Additionally, the post-second-order saddle dynamics revealed that most trajectories followed the minimum energy path, offering alternative pathways for cyclopropane formation with retention of the configuration. In contrast, trajectories initiated from asynchronous transition state regions mostly deviated from the minimum energy path, leading to longer-lived diazenyl diradicals while still favoring single inversion in the final products. Despite significant diradical lifetimes, trajectories from all six transition-state regions exhibited a preference for single inversion cyclopropane formation, suggesting that product selectivity is dictated by dynamical effects rather than the reaction pathway.

1 Introduction

Cyclopropanes are basic structural units found in many natural products and biologically active compounds that have important pharmaceutical applications. This makes them valuable in drug design and synthesis.[1–7] As a result, numerous methods have been devised to generate them in an optically pure state.[8–12] One of the methods widely used for the preparation of cyclopropane derivatives is the denitrogenation of 1-pyrazolines under thermal and photochemical conditions.[13–25] In this context, the mechanism of denitrogenation of 1-pyrazolines has been the subject of multiple studies in the gas phase,[16–18,26,27] solution phase,[19,20] and solid state.[24,25] It is now acknowledged that both thermal and photochemical denitrogenation involve diazenyl and/or trimethylene diradical intermediates.[19,28–30] The photochemical denitrogenation of 1-pyrazoline has been reported to follow a stepwise mechanism involving a trimethylene-type diradical intermediate, which closes more rapidly than the C–C bond rotations to form stereospecific cyclopropanes with retention of the configuration.[14,19,24,25,31]

In contrast, the thermal denitrogenation of 1-pyrazolines results in stereoselective products.[16,18,20–23,26,32] Various mechanisms have been proposed from several experimental and theoretical studies to explain the product selectivity. Crawford and Mishra[16] reported that thermal denitrogenation of *cis*- and *trans*-3,5-dimethyl-1-pyrazoline produced *trans*- and *cis*-1,2-dimethylcyclopropane, respectively, as the major product indicating inversion at one of the reacting carbon centers. They proposed a synchronous denitrogenation pathway leading to the trimethylene diradical intermediate followed by a conrotatory ring closure to explain the formation of the major single-inverted cyclopropane.

Subsequent studies, however, suggested complexities in the reaction mechanism. The stereochemically random ring closure observed during the thermolysis of cyclopropane[8,33–35] prompted Condit and Bergman[26] to investigate the thermal denitrogenation of *exo*- and *endo*-2-methyl-3,4-diazabicyclo[3.3.0]oct-3-enes. Their aim was to restrict the formation of a trimethylene diradical intermediate by attaching a short 3-carbon bridge to the C1 and C2 positions of 1-pyrazoline, thereby controlling the stereochemistry of the products. However, denitrogenation of both *exo*- and *endo*-2-methyl-3,4-diazabicyclo[3.3.0]oct-3-enes still resulted in a major single-inverted cyclopropane,[26] suggesting

School of Chemical Sciences, National Institute of Science Education and Research (NISER) Bhubaneswar, An OCC of Homi Bhabha National Institute, Khurda, Odisha, 752050, India. E-mail: u.lourderaj@niser.ac.in

† Electronic supplementary information (ESI) available: Potential energy profiles for synchronous and asynchronous pathways; plots of C–C bond distances and electron densities; plots of dihedral angles and C–N bond distances; plots of C–N bond distances *vs.* time; lifetime distribution plots for diradicals; matrix displaying number of inversions at carbon centers. See DOI: **https://doi.org/10.1039/d5cp00798d**

that denitrogenation in these molecules occurred through a sequential C–N cleavage mechanism.

Later, Bergman and coworkers[18] studied the denitrogenation of *cis*- and *trans*-3-ethyl-5-methyl-1-pyrazoline and proposed that the reaction involved the non-linear extrusion of N_2 by pseudo-conrotation of C–C bonds. A theoretical study by Jean and Hiberty[27] at the 3 × 3 CI/STO-3G level, for the thermal decomposition of 1-pyrazoline revealed that stepwise denitrogenation pathways *via trans* and *gauche* diradicals were energetically more favorable compared to the synchronous and non-linear extrusion pathways.

To gain deeper insights into the mechanisms, we recently mapped the potential energy profile for all possible denitrogenation pathways of 1-pyrazoline using CASSCF and CASPT2 methods with different basis sets.[36] In contrast to Jean and Hiberty's study,[27] we found that the synchronous denitrogenation pathway is energetically more favorable than the asynchronous pathways. The main cause of this discrepancy is possibly due to differences in the methodological treatment, since Jean and Hiberty[27] used a relaxed geometry scan to evaluate the energy barriers. The partially optimized transition state structures reported by them could not be obtained by full optimization at the CASSCF(4,4) level.[36] The synchronous denitrogenation of 1-pyrazoline leads to a trimethylene diradical intermediate, which undergoes ring closure to form cyclopropane *via* conrotatory or disrotatory rotation of the terminal methylene group. The barrier for conrotatory and disrotatory closure of the trimethylene diradical intermediate to cyclopropane is ∼1 kcal mol^{-1}. Consequently, if denitrogenation occurs synchronously, a racemic mixture of cyclopropane is expected.[37–39] Therefore, the formation of a major single-inverted cyclopropane observed experimentally could not be solely explained by the energetics of the reaction.

To investigate dynamic effects in the stereoselective formation of single-inverted cyclopropane, we conducted an *ab initio* classical trajectory study at the CASSCF level of theory for 1-pyrazoline and its substituted isotopomer *trans*-3,5-di-^{15}H-1-pyrazoline where an isotopic mass of 15 amu (to represent CH_3 group) was assigned to the H atoms.[40] The simulations revealed that out of 4000 trajectories integrated from the reactant region of 1-pyrazoline, 314 (7.85 ± 0.83%) were reactive. Denitrogenation occurred *via* both the synchronous and asynchronous paths, resulting in the major single-inverted cyclopropane consistent with the experimental findings. Additionally, the trajectories revealed a non-traditional second-order saddle (SOS) pathway (∼4%), which involved a planar second-order saddle point.

Although our study provided valuable insights into the overall reaction dynamics, statistically reliable data is still desirable to rationalize the nonstatistical product distribution and the pathways involved, particularly those related to the newly identified SOS pathway. In addition to improving trajectory statistics, the present study is focused on two key aspects: (i) the origin of the nonstatistical product distribution and (ii) the post-second-order saddle dynamics.

In an earlier study,[40] the origin of the nonstatistical product distribution observed in both experiments and simulations could not be conclusively determined. It is important to note that such distributions can arise due to incomplete intramolecular vibrational energy redistribution (IVR) before the system accesses the transition state regions, or due to dynamical effects associated with post-transition state (post-TS) dynamics, especially when intermediates are present along the reaction pathways. To address this, the current study investigates the post-TS dynamics of 1-pyrazoline denitrogenation from the synchronous and asynchronous transition state regions independently, in order to examine the dynamical effects influencing product selectivity. In addition, we examine the post-SOS dynamics by initiating trajectories from the SOS region. This approach is expected to improve statistical reliability and provide insights into the dynamics and product distribution associated with the SOS pathway.

2 Computational details

In our previous work,[36] we conducted a detailed study of the energetics underlying the thermal denitrogenation of 1-pyrazoline using the CASSCF and CASPT2 methods, employing various active spaces and the 6-31+G*, 6-311+G*, cc-pVDZ, aug-cc-pVDZ, and cc-pVTZ basis sets. We found that the CASSCF(4,4)/6-31+G* level of theory accurately describes the denitrogenation pathways when compared to benchmark CASPT2(12,12) energies. Therefore, the CASSCF(4,4)/6-31+G* level of theory was selected as the method of choice for the on-the-fly classical trajectory simulations performed in this study.

Ab initio classical trajectory simulations were performed by computing the forces on-the-fly at each step using the CASSCF(4,4)/6-31+G* level of theory.[41–45] The active space for the CASSCF(4,4) calculations involved the σ and σ* orbitals of both the C–N bonds. Initial coordinates and momenta for the trajectory simulations were selected using the microcanonical normal mode sampling procedure.[46]

Batches of 300 trajectories were initiated independently from the synchronous and various asynchronous transition state regions, with an excess energy of (E_{tot} − E_a) kcal mol^{-1}, where E_{tot} is the energy available to the reactant 1-pyrazoline, and E_a corresponds to the classical energy barrier of the respective transition state. The total energy (E_{tot}) was calculated as follows: among the different pathways mapped for the denitrogenation of 1-pyrazoline,[36] the transition state **TS4f** corresponding to the asynchronous step-wise path, had the highest barrier of 52.84 kcal mol^{-1} (Fig. S1–S4, ESI†). Assuming a Boltzmann distribution of energies at **TS4f** for the experimental temperature (510.45 K),[16] the excess energy available to **TS4f** was calculated as $E_{excess} = E_{zpe} + E_{vib} + E_{rot} + E_{rc}$, where E_{zpe}, E_{vib}, and E_{rot} are the zero-point-energy, average vibrational energy, and average rotational energy of **TS4f**, respectively. The energy along the reaction coordinate, E_{rc}, was taken as RT. The total energy of the reactant was then calculated as $E_{tot} = E_{\mathbf{TS4f}} + E_{excess}$, yielding a value of 119.10 kcal mol^{-1}.

Additionally, 300 trajectories were initiated from the **SOS** region, with an excess energy of (E_{tot} − E_{SOS}) kcal mol^{-1} to investigate post-second-order saddle dynamics, where E_{SOS} = 44.12 kcal mol^{-1} is the SOS energy. Initial coordinates and

momenta for these trajectories were selected using the micro-canonical normal mode sampling procedure described in our previous work.[47] All classical trajectory calculations were performed using a modified version of VENUS/NWChem[48,49] on an Intel(R) Xeon(R) CPU E5-2697A v4@2.60 GHz computer. The trajectories were integrated using the velocity-Verlet algorithm with a step size of 0.3 fs over a total simulation time of 1 ps.

3 Results and discussion

3.1 Denitrogenation pathways

We recently reported in detail the various denitrogenation pathways for 1-pyrazoline obtained using the CASSCF and CASPT2 methods.[36] Here, we discuss these pathways for completeness in the context of the present study. Fig. 1 provides a summary of the denitrogenation paths obtained for the thermal denitrogenation of 1-pyrazoline at the CASSCF(4,4)/6-31+G* level of theory. The thermal denitrogenation of 1-pyrazoline can happen *via* three different pathways.

(a) Synchronous denitrogenation. The synchronous denitrogenation path involves the simultaneous breaking of both C–N bonds through the transition state **TS1**, leading to the formation of a trimethylene diradical intermediate, **Int1**. **Int1** can then close to cyclopropane *via* con- or dis-rotation of the terminal methylene groups or can form alkene through proton migration. Conrotatory closure of the terminal methylene groups of **Int1** results in single-inverted (SI) cyclopropane, while disrotatory closure leads to cyclopropane with double inversion (DI) or retention (Ret) of the configuration. A flipping motion of the central methylene (CH_2) group connects **TS1** to the symmetric transition state **TS1′** *via* a second-order saddle point **SOS**, from which the dissociation of N_2 can occur directly (Fig. S1, ESI†).

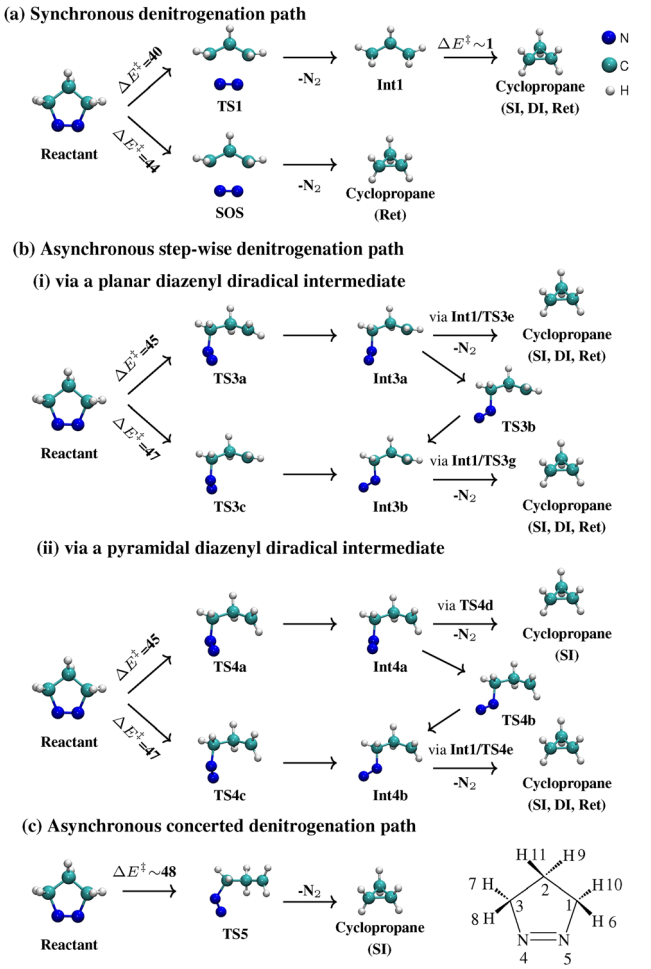

Fig. 1 Summary of the possible denitrogenation paths, (a)–(c), obtained for the thermal denitrogenation of 1-pyrazoline at the CASSCF(4,4)/6-31+G* level of theory.

(b) Asynchronous step-wise denitrogenation. This pathway involves the breaking of one of the C–N bonds to form the diazenyl diradical (DZ) intermediate, followed by the breaking of the other C–N bond. Since, the PES is symmetrical about the C–N bond cleavage, the asynchronous cleavage of either C1–N5 or C3–N4 bonds would result in similar structures. Here, we discuss the pathways where the C1–N5 bond is cleaved first. Two distinct paths for the asynchronous cleavage of the C1–N5 bond of 1-pyrazoline were identified, depending on the type of diazenyl diradical intermediate formed (Fig. S2 and S3, ESI†).[36]

(i) Pathways *via* a planar-like diazenyl diradical intermediate. In this path, a planar diazenyl diradical intermediate **Int3a** is formed *via* the transition state **TS3a** through the anti-clockwise rotation of the C3–N4 bond. The terminal methylene group of the diazenyl diradical has a planar-like geometry ($\angle$C3C2C1H6 $\sim -44^\circ$, $\angle$C3C2C1H10 $\sim 157^\circ$). From **Int3a**, free rotation of the N_2 group about the C3–N4 bond can occur, leading to the formation of **Int3b** *via* **TS3b**, and subsequently returning to the reactant with further rotation through **TS3c**. Thus, **Int3b** can also be accessed by clockwise rotation of the C3–N4 bond *via* **TS3c**. The dissociation of the second C–N bond (C3–N4) can occur from either **Int3a** or **Int3b** with simultaneous closure of the three-membered ring to form SI cyclopropane. Alternatively, breaking the second C–N bond may lead to the formation of **Int1**, which can subsequently close to cyclopropane with SI, DI, or Ret configurations.

(ii) Pathways *via* a perpendicular-like diazenyl diradical intermediate. Anti-clockwise rotation of the C3–N4 bond can also yield a diazenyl diradical that has a perpendicular-like geometry ($\angle$C3C2C1H6 $\sim -72^\circ$, $\angle$C3C2C1H10 $\sim 90^\circ$) *via* **TS4a**. Similar to the pathways involving the planar-like diazenyl diradical intermediate, rotation of the N_2 group about the C3–N4 bond generates the rotational isomers **Int4b** and **Int4f**. From these intermediates, SI cyclopropane can form directly, or cyclopropane with SI, DI, or Ret configurations can form *via* **Int1**. While **Int4b** and **Int4f** are connected to each other by **TS4f**, **Int4b** can also return to the reactant *via* **TS4c**.

(c) Asynchronous concerted denitrogenation. This pathway involves the asynchronous breaking of one of the C–N bonds, specifically the C1–N5 bond, *via* the transition state **TS5**. It leads to the formation of cyclopropane with an SI configuration (Fig. S4, ESI†).

From the potential energy profiles, the following observations can be made: (i) synchronous and asynchronous stepwise

denitrogenation of 1-pyrazoline results in cyclopropane with SI, DI, and Ret configurations, and (ii) asynchronous concerted denitrogenation of 1-pyrazoline results in cyclopropane with an SI configuration. The asynchronous concerted path has an energy barrier ($\Delta E^{\ddagger}$ = 48.21 kcal mol^{-1}) approximately 8 kcal mol^{-1} higher than the synchronous pathway and about 1–3 kcal mol^{-1} higher than the stepwise asynchronous pathway. Energetically, the synchronous pathway is the most favorable, yielding cyclopropane with SI, DI, and Ret configurations. However, the experimental observation of a major SI cyclopropane indicates that dynamical effects play a crucial role in determining product selectivity. Below, we discuss the results of the *ab initio* classical trajectory simulations performed from different transition state regions to elucidate the dynamics and mechanisms of the denitrogenation reaction.

3.2 Trajectories initiated from the synchronous transition state (TS1) region

The transition state vector for the synchronous path transition state **TS1** involves simultaneous stretching of both the C–N bonds. A total of 300 trajectories were initiated randomly from the **TS1** region. The statistics of the products formed in these trajectories are given in Table 1. Out of 300 trajectories, 101 returned to the reactant, 198 led to cyclopropane (**Cp**), and one resulted in an alkene. From **TS1**, 163 of 198 trajectories form **Cp**, while the remaining 35 trajectories form the reactant first and subsequently recross the TS region to form **Cp**. Among these 35 recrossing trajectories, 21 dissociated *via* the synchronous denitrogenation pathway, while 14 followed the asynchronous pathway. Since the focus is on understanding the post-transition-state dynamics, the 35 recrossing trajectories were excluded from the product analysis. Consequently, the analysis was performed on the remaining 163 trajectories. Of these, 86 (52.7%) formed SI cyclopropane, 59 (36.2%) formed DI cyclopropane, and 18 (11.0%) formed cyclopropane with retention of the configuration.

Table 1 Number of trajectories forming reactants (**R**), propylene (**Py**), **Int1**, and **Cp**, and those exhibiting recrossing, for sets of 300 trajectories integrated from **TS1**, **SOS**, **TS3a**, **TS3c**, **TS4a**, **TS4c**, and **TS5** regions[a]

					Cp			
Region	R	Py	Int1	Recrossing R → Cp	SI	DI	Ret	Total
TS1	101	1		35	86 53%	59 36%	18 11%	163
SOS	63	1	1	18	54 24.9%	60 27.6%	103 47.5%	217
TS3a	26			3	123 45%	79 29%	69 25%	271
TS3c	20			8	137 50%	76 28%	59 22%	272
TS4a	36		1	22	124 51%	55 23%	62 26%	241
TS4c	7		1	4	147 51%	103 36%	38 13%	288
TS5	10			2	189 65.6%	53 18.4%	46 16%	288
Experiment[18 b]					73%	16%	10%	

[a] The fraction of trajectories forming different products are also given as percentages. [b] The experimental data is for *trans*-3,5-dimethyl-1-pyrazoline.

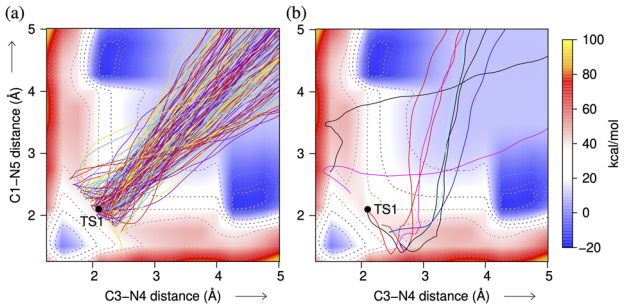

Fig. 2 Plot of the C1–N5 and C3–N4 distances for all trajectories initiated from the **TS1** region following (a) synchronous and (b) asynchronous denitrogenation pathways. The trajectories are projected onto a two-dimensional PES obtained from a relaxed scan of the C–N distances for 1-pyrazoline.

To determine whether the denitrogenation process was synchronous or asynchronous, the changes in C3–N4 and C1–N5 bond distance over time were monitored for the 163 trajectories. Of these, 154 trajectories (Fig. 2(a)) dissociated *via* the synchronous denitrogenation pathway, while the remaining 9 trajectories (Fig. 2(b)) followed an asynchronous path despite starting from the synchronous transition-state region. A plot of the angle ∠C1–C2–C3–N4 *versus* the C3–N4 distance (Fig. 3) reveals that most trajectories followed the minimum energy path (MEP). All trajectories dissociating from **TS1** formed the trimethylene diradical intermediate (**Int1**), which either closed to form **Cp** or formed an alkene without ring closure. Interestingly, six trajectories were found to dissociate from the **SOS** region.

To investigate the observed experimental product selectivity, the atomic-level mechanisms from **TS1** to **Cp** by the ring closure of **Int1** were followed for the 154 synchronous trajectories. The stereochemistry of cyclopropane obtained is expected to be influenced by the lifetime of **Int1** (*i.e.*, how long the system remains in the diradical region) and the number of rotations of the terminal methylene groups before closure.

We calculated the lifetime of the diradical intermediate **Int1** by tracking the electron densities of the σ_{C-N} and σ_{C-N}* orbitals during dissociation for all trajectories. An electron density greater than 0.45 on the σ_{C-N}* orbital was used as the criterion

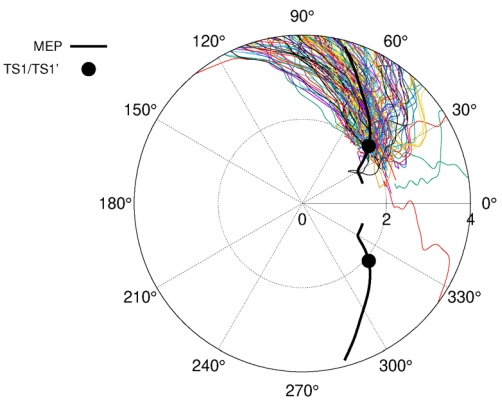

Fig. 3 Polar plot of ∠C1–C2–C3–N4 *vs.* C3–N4 distance for **TS1**, **TS1′**, IRC path (MEP), and the 163 trajectories that form **Cp** from **TS1**.

for a radical. The lifetime distribution of the trimethylene diradicals (Fig. S5(a), ESI†) exhibited an exponential decay, with an initial equilibration time of ~100 fs. The average lifetime of the diradical was found to be 128 fs, comparable to the experimental lifetime value of 120 ± 20 fs observed for cyclopropane isomerization.[50]

Since the barrier for the rotation of the terminal methylene groups in **Int1** is ~1 kcal mol^{-1}, these groups can rotate multiple times before closing to form **Cp**. The number of rotations of the terminal methylene groups corresponding to the C1 and C3 atoms was calculated by monitoring the dihedral angles ∠C3C2C1H6 and ∠C1C2C3H8 over time. These rotations were denoted as (n_{C1},n_{C3}). The number of terminal methylene rotations and the average lifetimes of the trimethylene diradical intermediate, obtained from 154 trajectories, are shown in Fig. S5(b) and (c) (ESI†). As seen in Fig. S5(b) (ESI†), the majority of the trajectories exhibit (0, 0), (0, 1), (1, 0), or (1, 1) rotations in the terminal methylene groups. When compared to trajectories with (1, 0), (0, 1), or (1, 1) rotations, the average lifetime of trajectories with (0, 0) rotation is shorter (86 fs), indicating that shorter **Int1** lifetimes favor the formation of **Cp** with retention of the configuration. The maximum inversion observed was (2, 7) in a trajectory that spent 359 fs in the **Int1** region before forming **Cp**.

It is interesting to look at the nature of the HOMO and LUMO during the reaction. The HOMO and LUMO of the stationary points **TS1**, **Int1**, and **Cp** along the MEP of synchronous denitrogenation are shown in Fig. 4(a). At **TS1**, the HOMO and LUMO are σ_{C-N} bonding and σ_{C-N}* anti-bonding orbitals, respectively. These orbitals change to p-type orbitals on the C1 and C3 atoms in **Int1** and subsequently to σ_{C-C} and σ_{C-C}* of the C1–C3 bond in **Cp**. Fig. 4(b)–(d) show the plots of the C1–C3 bond distance and the electron densities of the σ_{C-N} and σ_{C-N}* orbitals *versus* time. We can see that the initial electron densities in the σ_{C-N} (ρ_1) and σ_{C-N}* (ρ_2) orbitals are ~1.6 and ~0.4, respectively. During the course of the reaction, ρ_1 decreases and ρ_2 increases until the diradical is formed when ρ_1 and ρ_2 are ~1.0. During the cyclopropane formation from the diradical, since the pπ and pπ* orbitals change their character to σ_{C-C} (ρ_1) and σ_{C-C}* (ρ_2) orbitals, ρ_1 and ρ_2 now become ~2.0 and ~0, respectively.

Detailed analysis of the C1–C3 bond distance and orbital electron densities revealed two trajectory types. In **Type 1** trajectories (Fig. 4(b)), the dissociation of the C–N bonds and the C1–C3 bond closure occur simultaneously. The system traverses the diradical region and the products are formed within 100 fs. All of the **Type 1** trajectories either undergo (0, 0), (0, 1), (1, 0), or (1, 1) inversions at the C1 and C3 carbon atoms. 43 (55.1%) of the 78 **Type 1** trajectories close to form SI cyclopropane, 26 (33.3%) form DI cyclopropane, and 9 (11.5%) form **Cp** with retention of the configuration. In **Type 2** trajectories (Fig. 4(c)), the system remains in the diradical region for a longer time before closing to **Cp**. These trajectories show multiple inversions at the C1 and C3 carbon centres. 37 (48.7%) out of 76 **Type 2** trajectories close to form SI cyclopropane, 31 (40.8%) form **Cp** with double inversion, and 8 (10.5%) trajectories form **Cp** with the retention of the configuration.

It is clear that **Type 1** trajectories with shorter **Int1** lifetimes have a higher preference for the formation of SI cyclopropane than **Type 2** trajectories. In contrast, prolonged residence of the system in the **Int1** region, facilitates efficient IVR reducing the preference for the formation of SI **Cp** relative to DI **Cp**. Only ~11% of trajectories close to **Cp** with the retention of the configuration. Additionally, 14 trajectories exhibited cyclopropane isomerization, involving ring opening and subsequent reclosure (Fig. 4(d)).

3.3 Post-second-order saddle dynamics

The dynamical simulations from the reactant (1-pyrazoline)[40] revealed that about 7% of the trajectories undergoing synchronous denitrogenation followed the **SOS** path. Therefore, it is of interest to explore the post-second-order saddle dynamics from the **SOS** region to understand the atomic-level mechanisms and their importance in product selectivity. To this end, we computed

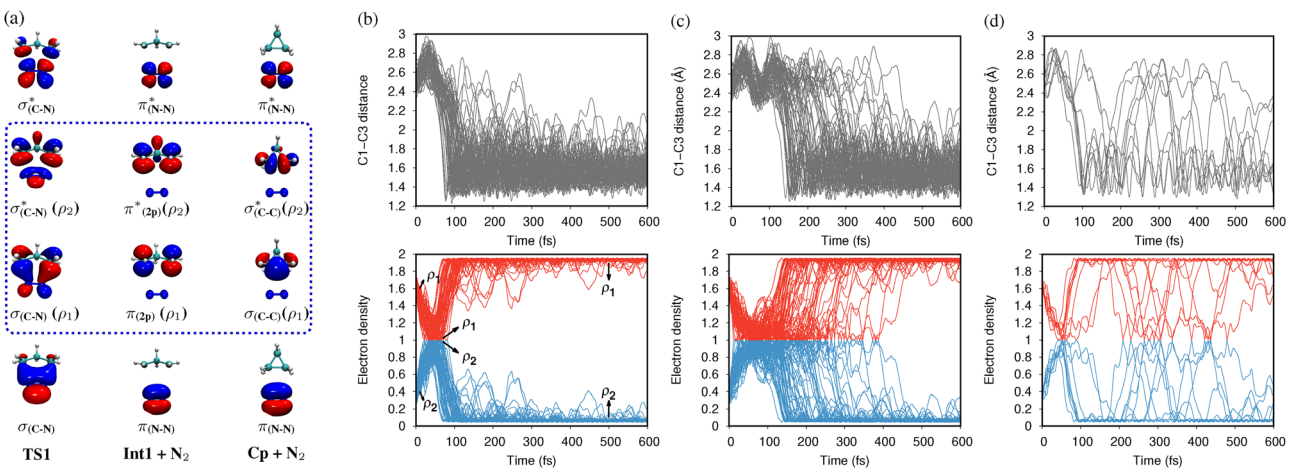

Fig. 4 (a) Orbital correlation diagram for the synchronous denitrogenation path from **TS1** to **Int1** and **Cp**. Plot of C1–C3 bond distance (top panel) and electron densities (ρ_1 and ρ_2, bottom panel) in the σ_{C-N} and σ_{C-N}* orbitals *vs.* time for trajectories initiated at the **TS1** region for (b) Type 1 trajectories with a short diradical lifetime, (c) Type 2 trajectories with a longer diradical lifetime, and (d) trajectories showing **Cp** isomerization.

300 trajectories initiated at the **SOS** region by assuming a microcanonical distribution of energies among all modes, with an excess energy of 74.98 kcal mol^{-1} available at the **SOS**.

Out of 300 trajectories, 235 resulted in **Cp**, 1 trajectory yielded an alkene, 1 trajectory was trapped in the **Int1** region for the integration time, and the remaining 63 trajectories returned to the reactant. From the **SOS**, 217 of the 235 trajectories formed **Cp**, while the remaining 18 formed the reactant first and subsequently recrossed the **SOS** region to form **Cp**. Of the 217 products formed, 54 (24.9%) resulted in the SI configuration, 60 (27.6%) gave the DI configuration, and 103 (47.5%) gave the Ret configuration. As observed in our previous study,[40] this clearly indicates that the **SOS** path provides an alternative mechanism for the formation of a major retention of the configuration product.

The mechanisms followed by the 235 reactive trajectories can be classified into the following four pathways (Fig. 5): (i) **SOS** → **Cp** (directly or *via* **Int1**). 217 of the 235 trajectories move in the forward direction from the **SOS** region to form **Cp** directly, or form **TMD**, which then results in **Cp**. (ii) **SOS** → **TS0** → **R** → **TS1** → **Cp**. One trajectory passes the **TS0** region and then forms **Cp** *via* the **TS1** region. (iii) **SOS** → **TS0** → **R** → **SOS** → **Cp**. Two trajectories first form the reactant from **SOS** and then form **Cp** after recrossing the **SOS** region. (iv) **SOS** → **R** → **TS1**/**TS1′** → **Cp**. 14 trajectories first form the reactant and then proceed *via* **TS1**/**TS1′** to form **Cp**. Interestingly, one trajectory follows the asynchronous path after forming the reactant from the **SOS** region.

The diradical lifetime distribution and the number of inversions (n_{C1}, n_{C3}) at the C1 and C3 atoms for the 217 trajectories that directly form **Cp** from the **SOS** region are shown in Fig. S6 (ESI†). We can see that most of the trajectories (98/217) have (0, 0) inversions at the C1 and C3 carbon atoms, resulting in the formation of **Cp** with retention of the configuration and have an average diradical lifetime of 60 fs.

Along the dissociation path from the **SOS**, the changes in electron densities of the C–N σ and σ* orbitals were tracked for the 217 trajectories. In 150 of the 217 trajectories, C–N dissociation and C1–C3 bond closure occur simultaneously, and **Cp** is formed within 100 fs (Fig. S7(a), ESI†). The remaining 67 trajectories spend more time in the diradical region (Fig. S7(b), ESI†).

It is interesting to look at the stereochemistry of **Cp** formed from these trajectories. For the trajectories that spent less than 100 fs in the diradical region, 25/150 (17%) gave SI **Cp**, 30/150 (20%) gave DI **Cp**, and 95/150 (63%) resulted in **Cp** with retention of the configuration. For the 67 trajectories that spent more time in the diradical region, 29 (43%) gave SI **Cp**, 30 (45%) gave DI **Cp**, and only 8 (12%) gave **Cp** with retention of the configuration.

As seen above, the trajectories that spend less time in the diradical region have a higher preference for the formation of **Cp** with retention of the configuration. Trajectories that spend longer time in the diradical region produce a racemic mixture of SI and DI **Cp**, with only 12% of them resulting in **Cp** with retention of the configuration, which is similar to the results observed for trajectories initiated in the **TS1** region. In 34 trajectories, the **Cp** formed from **SOS** undergoes ring isomerization (Fig. S7(c), ESI†).

3.4 Trajectories integrated from the asynchronous step-wise transition state regions

We computed sets of 300 trajectories, initiated from each of the four asynchronous stepwise path transition states (**TS3a**, **TS3c**, **TS4a**, **TS4c**), using a microcanonical sampling procedure. The transition states connect the reactant and diazenyl diradicals. The transition state vector associated with **TS3a**, **TS3c**, **TS4a**, and **TS4c** corresponds to simultaneous stretching of the C1–N5 bond and torsional motion about the C3–N4 bond (∠C2–C3–N4–N5 angle). Table 1 summarizes the outcomes of the trajectories integrated from the different asynchronous stepwise transition states.

As shown in Table 1, the trajectories follow four distinct paths: (i) formation of the reactant, **R**, (ii) remaining in the **Int1** region throughout the integration time, (iii) initial formation of the reactant followed by recrossing the transition state region to form **Cp**, and (iv) formation of **Cp** *via* different intermediates. Recrossing trajectories were excluded from the product analysis. The table shows that the majority of trajectories originating from the four transition states result in the formation of **Cp**, primarily with the SI configuration, followed by double inversion and retention of the configuration.

We further investigated the atomic-level mechanisms underlying the formation of **Cp**. In transitioning from the reactant to **Cp** *via* the asynchronous stepwise transition states along the MEP, the N_2 group undergoes a clockwise/anticlockwise rotation about the C3–N4 bond concurrent with the dissociation of

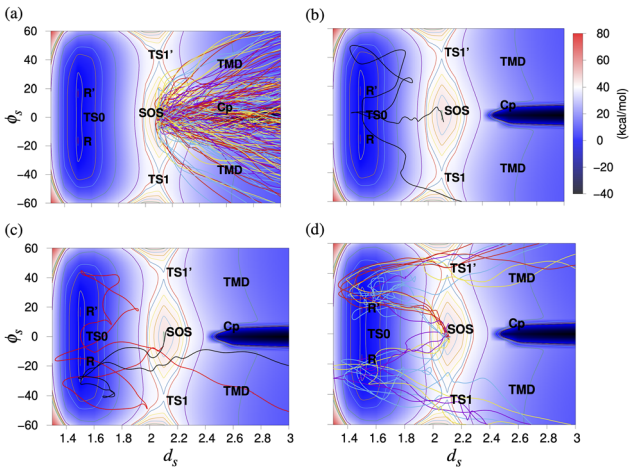

Fig. 5 Plot of ϕ_S (°) and d_S (Å) for (a) 217 trajectories projected on the relaxed PES for the synchronous path for 1-pyrazoline. These trajectories move in the forward direction towards **Cp**/**TMD** from the **SOS** region, (b) one trajectory that first goes to **TS0** from the **SOS** region, forms the reactant, and then passes through **TS1** forming **Cp**, (c) two trajectories that first form the reactant from the **SOS** region and then form **Cp** *via* **SOS**, and (d) 14 trajectories that first form the reactant from the **SOS** region and then form **Cp** *via* **TS1** or **TS1′**. $\phi_S = (\phi_1 - \phi_2)/2$, where ϕ_1 and ϕ_2 are the dihedral angles ∠C1C2C3N4 and ∠C3C2C1N5, and d_S is the mean of the two C–N bond distances.

the C1–N5 bond. In the transition states, the C1–N5 bond is already broken and it is of interest here to understand the process of C3–N4 bond breaking from the transition states.

If trajectories follow the MEP, the C3–N4 bond can dissociate from **Int3a**/**Int4a** or **Int3b**/**Int4b**. However, due to the presence of excess kinetic energy, trajectories may deviate from the MEPs and follow dynamically driven pathways. To investigate the mechanism of C3–N4 bond dissociation, we tracked changes in the ∠C2–C3–N4–N5 dihedral angle as a function of the C3–N4 bond distance across all trajectories.

The polar plot of the dihedral angle ∠C2–C3–N4–N5 *vs.* C3–N4 bond distance for the MEP and 271 **TS3a** trajectories that form **Cp** is shown in Fig. 6. We can see that the trajectories follow various dynamical reaction pathways that deviate from the MEP, with the C3–N4 bond dissociating at varying ∠C2–C3–N4–N5 values. Based on the dissociation patterns, trajectories were classified into six categories. Fig. 6(a) shows 69 trajectories that dissociate directly from the **TS3a** region without passing through the DZ intermediates. Fig. 6(b) depicts 62 trajectories proceeding to the diradical intermediate **Int3a** from **TS3a**, where the C3–N4 bond subsequently dissociates. In 40 trajectories, the N_2 group rotates clockwise or anticlockwise about the C3–N4 bond, closely following the MEP, and the C3–N4 bond later dissociates *via* the **TS3b** region, as shown in Fig. 6(c). Similarly, the C3–N4 bond dissociates from the **Int3b** and **TS3c** regions in 14 and 10 trajectories, respectively, as shown in Fig. 6(d) and (e).

In 76 trajectories, the N_2 group rotates clockwise about the C3–N4 bond, accompanied by the dissociation of the C3–N4 avoiding the **TS3c**/**Int3b** region (Fig. 6(f)), taking a non-IRC route to form **Cp**. In one trajectory, the N_2 group completes a 360° rotation about the C3–N4 bond before its dissociation. Notably, the stationary points **TS3a**, **TS3b**, and **TS3c** are not directly connected to the diradical **Int1** or the product **Cp**, making direct C3–N4 bond cleavage from these regions a dynamical pathway that avoids MEPs.

We performed a similar analysis for the trajectories initiated from the **TS3c**, **TS4a**, and **TS4c** regions and the corresponding ∠C2–C3–N4–N5 *vs.* C3–N4 bond distance plots are shown in Fig. S8–S10 (ESI†), respectively. Table 2 outlines the mechanisms of C3–N4 bond dissociation followed by the trajectories integrated from the four asynchronous step-wise transition states **TS3a**, **TS3c**, **TS4a**, and **TS4c**. We can see that only 76, 48, 69, and 45 trajectories integrated from **TS3a**, **TS3c**, **TS4a**, and **TS4c**, respectively, exhibit C3–N4 bond dissociation from the **Int3a**/**Int4a** or **Int3b**/**Int4b** regions of the PES following the MEP. For these 76, 48, 69, and 45 trajectories, a plot of ∠C1C2C3N4 bond angle *vs.* C3–N4 bond distance reveals that the C3–N4 bond dissociates either directly from **Int3a** and **Int3b** (Fig. 7(a) and (b), and Fig. S11–S13, ESI†) *via* the transition states **TS3d** and **TS3f**, respectively, or *via* an S_H2-like mechanism through the transition states **TS3e**/**TS4d** and **TS3g**/**TS4e**, respectively. In the S_H2-like mechanism, the axial N_2 group of the DZ radical changes to the equatorial position, followed by the C3–N4 bond

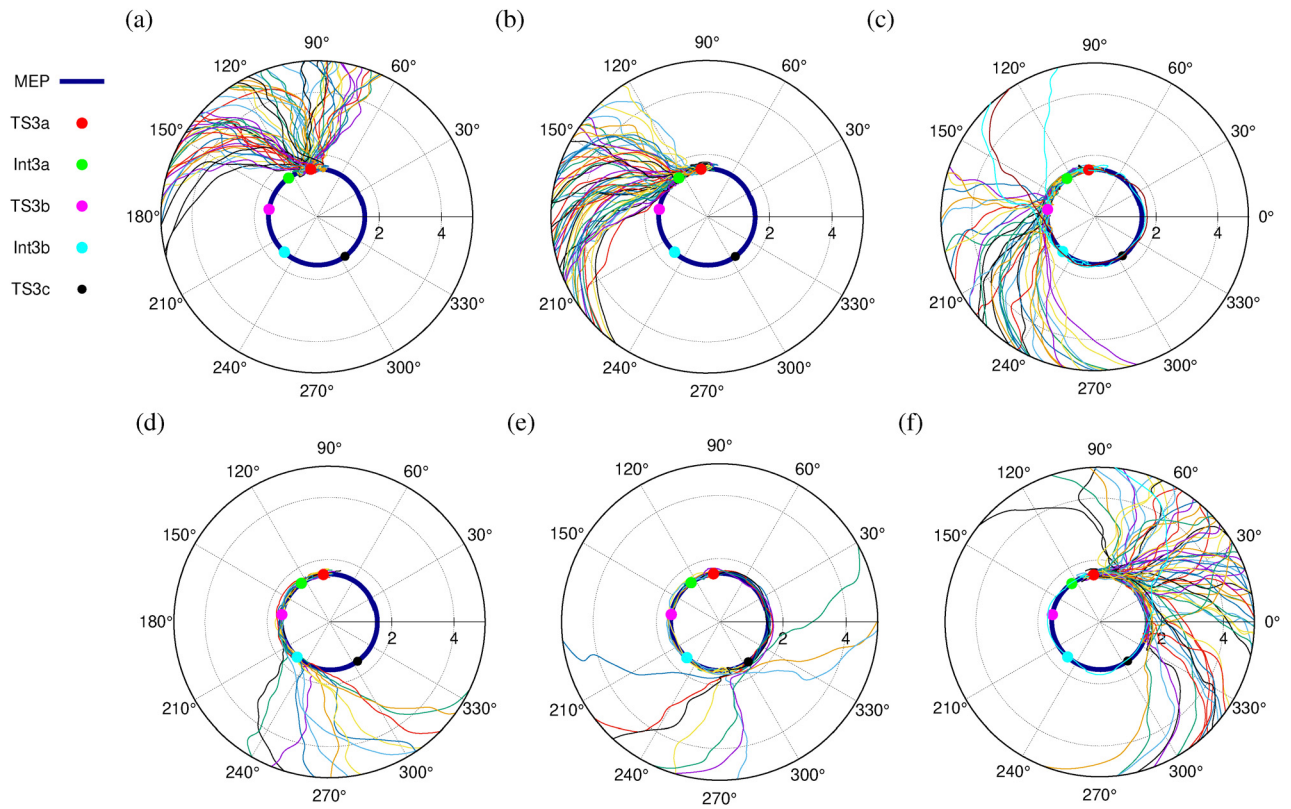

Fig. 6 Plot of ∠C2–C3–N4–N5 *vs.* C3–N4 for the minimum energy path, all the stationary points along the minimum energy path, and the 271 trajectories that form **Cp** from the transition state **TS3a**, following different dynamical pathways (a) to (f).

Table 2 The atomic level mechanisms of C3–N4 bond dissociation followed by trajectories integrated from **TS3a**, **TS3c**, **TS4a**, and **TS4c** regions

TSs	Int3a/Int4a	Int3b/Int4b	TS3a/TS4a	TS3b/TS4b	TS3c/TS4c	Non-IRC region
TS3a	62	14	69	40	10	76
TS3c	8	40	7	19	161	37
TS4a	54	15	121	26	5	20
TS4c	9	36	5	15	158	65

dissociation to yield SI **Cp** (See Fig. S2, and S3, ESI†). A similar S_H2 mechanism was proposed to explain the substantial stereochemical inversion in housane formation in the photochemical denitrogenation of diazabicycloheptene.[51]

Fig. 7 presents snapshots of two sample trajectories integrated from the **TS3a** region. In the first trajectory (Fig. 7(c)), the C3–N4 bond dissociates directly from the **TS3a** region, and **Cp** forms in approximately 225 fs. In the second trajectory (Fig. 7(d)), the N_2 group dissociates *via* the S_H2-like transition state **TS3g**. Here, the terminal methylene group (CH_2) completes a 360 rotation in about 145 fs, after which the N_2 group rotates about the C–N bond in tandem with the rotation of both CH_2 groups until ~205 fs to form **Int3b**. The N_2 group of **Int3b** subsequently transitions from an axial to an equatorial position around 300 fs, after which the N_2 group dissociates, forming **Cp**.

Since asynchronous trajectories pass through both the DZ and TMD diradical regions, the amount of time the system spends in these regions influences the stereochemistry of the **Cp** formed. To investigate this, we calculated the total diradical lifetime and the individual lifetimes of the DZ and TMD diradicals by monitoring the electron densities of the HOMO and LUMO orbitals during the dissociation process. The C–N bond lengths were used to distinguish the lifetimes of the DZ and TMD diradicals. When both C–N distances exceed 4.5 Å, the diradical is designated as TMD. This threshold was selected because the longest C–N distance corresponding to the TSs along the asynchronous paths is approximately 4.5 Å.

Fig. S14–S17 (ESI†) present the plots of the C3–N4 bond distance *versus* time and the difference in electron density between the HOMO and LUMO orbitals during the dissociation process for the **TS3a, TS3c, TS4a,** and **TS4c** trajectories following different pathways, respectively. In most trajectories that dissociate directly from the transition state regions from which they are integrated, the dissociation of the C3–N4 bond and the closure of the C–C bond occur simultaneously, forming **Cp** within 200 fs. As the trajectories explore the DZ region of the PES, their lifetimes increase.

Fig. S18–S21 (ESI†) show the distribution of the total diradical lifetimes (DZ + TMD), the diazenyl diradical lifetimes,

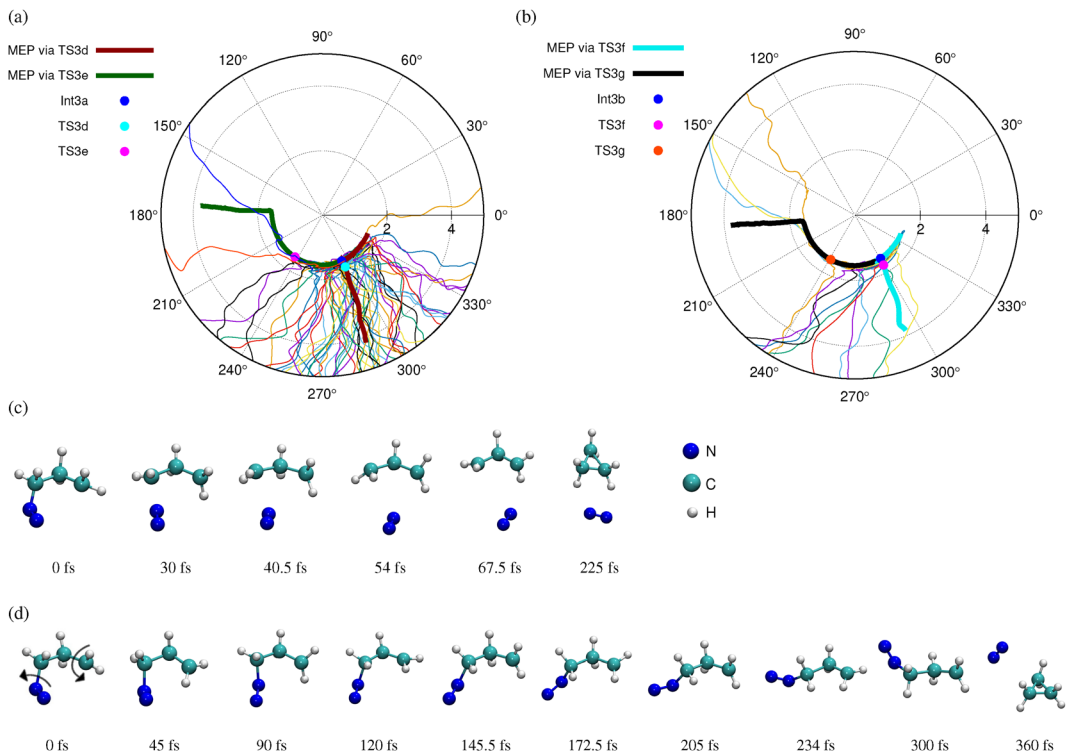

Fig. 7 Plots of ∠C1–C2–C3–N4 *versus* C3–N4 for the minimum energy path, all stationary points along the minimum energy path, and the **TS3a** trajectories that dissociate from the (a) **Int3a** and (b) **Int3b**. (c) Snapshots of a sample trajectory in which the C3–N4 bond dissociates in the **TS3a** region of the PES. (d) Snapshots of a trajectory in which the N_2 group rotates 273 around the C3–N4 bond before dissociating *via* the S_H2-like transition state **TS3g**.

and the trimethylene diradical lifetimes for the **TS3a**, **TS3c**, **TS4a**, and **TS4c** trajectories, respectively. The total lifetime distributions exhibit a nearly exponential decay, with an initial equilibration time of approximately 150 fs, and the average total lifetimes were 206 fs, 192 fs, 199 fs, and 178 fs for the **TS3a**, **TS3c**, **TS4a**, and **TS4c** trajectories, respectively. Notably, the diazenyl diradicals are longer-lived compared to the TMD radicals and account for the majority of the diradical lifetimes.

Additionally, we calculated the number of inversions at the C1 and C3 stereocenters. Fig. S22 (ESI†) illustrates the number of inversions at the C1 and C3 stereocenters before forming **Cp** for the **TS3a**, **TS3c**, **TS4a**, and **TS4c** trajectories. The majority of these trajectories undergo (0, 0), (0, 1), (1, 0), and (1, 1) inversions at the stereocenters. For **TS3a**, **TS3c**, and **TS4a** trajectories, the major SI **Cp** product arises primarily from inversion at the C1 center, whereas for **TS4c** trajectories, the major SI **Cp** results largely from inversion at the C3 center.

3.5 Trajectories initiated from the asynchronous concerted transition state (TS5) region

The reaction coordinate vector for **TS5** involves the stretching of the C1–N5 bond and the torsional motion of ∠C1–C2–C3–N4. At **TS5**, the C1–N5 bond length is 3.8 Å, and the ∠C1–C2–C3–N4 is −112.33°. A total of 300 trajectories were initiated from the **TS5** region using microcanonical normal mode sampling of states with an energy of 70.89 kcal mol^{-1}. Of these, 10 trajectories lead to the reactant, while 290 resulted in **Cp**. Among the reactive trajectories, 288 proceeded directly from the TS region to form **Cp**, while the remaining 2 initially access the reactant region before recrossing the TS region to form **Cp**.

Out of the 288 trajectories, 189 (65.6%) yield SI **Cp**, 53 (18.4%) result in DI **Cp**, and 46 (16.0%) produce **Cp** with retention of the configuration. The preference for SI **Cp** formation observed in the **TS5** trajectories aligns with the product stereochemistry experimentally reported for *trans*-3,5-dimethyl-1-pyrazoline.[16,18]

To investigate the mechanism of **Cp** formation from the transition state region, we monitored ∠C1–C2–C3–N4 and ∠C2–C3–N4–N5 as functions of the C3–N4 bond distance during the trajectories. Fig. 8(a) and (b) illustrate the changes in ∠C2–C3–N4–N5 *versus* C3–N4 bond distance and ∠C1–C2–C3–N4 *versus* C3–N4 bond distance for the MEP, **TS5**, and the 288 trajectories that form **Cp** from **TS5**, respectively. Most trajectories dissociate directly from the **TS5** region of the PES, forming **Cp** following the MEP. The rest of the trajectories follow various dynamical paths that deviate from the MEP associated with **TS5**. In these cases, the C3–N4 bond dissociates at different ∠C2–C3–N4–N5 and ∠C1–C2–C3–N4 angles follow the asynchronous, stepwise denitrogenation pathway (Fig. 8(a)), even though they were initiated from the **TS5** region.

To further explore the mechanism of **Cp** formation from **TS5**, we calculated the total diradical lifetime and the individual lifetimes of the DZ and TMD diradicals by monitoring the electron densities of the HOMO and LUMO orbitals during the dissociation process. Fig. S23 (ESI†) shows the correlation between the number of (n_{C1}, n_{C3}) rotations and the time spent

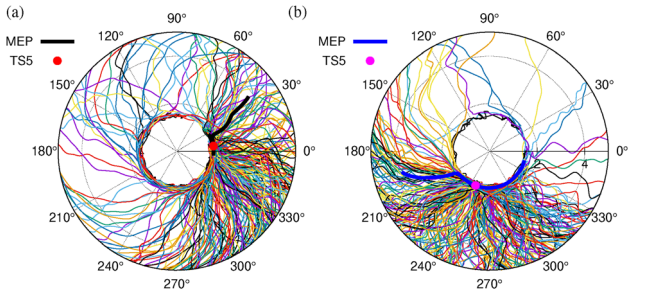

Fig. 8 Polar plots of (a) ∠C2–C3–N4–N5 *versus* C3–N4 bond distance and (b) ∠C1–C2–C3–N4 *versus* C3–N4 bond distance for **TS5**, MEP, and the 288 **TS5** trajectories that form **Cp**.

in the DZ and TMD diradical regions. As illustrated in Fig. S23(a) (ESI†), the lifetime distribution exhibits an initial equilibration time followed by an exponential decay with an average lifetime of 138.32 fs. The majority of trajectories involve inversions at the C3 carbon center ((0,1) inversion), leading to the formation of SI **Cp**. Fig. S23(c) and (d) (ESI†) indicate that the system spends most of its time in the DZ diradical region of the PES, briefly passing through the TMD region prior to forming **Cp**.

Interestingly, the average diradical lifetime for trajectories showing (0,1) inversion is the shortest (56 + 9 = 65 fs). This contrasts with trajectories integrated from the synchronous and asynchronous stepwise transition state regions, where trajectories showing (0,0) inversion exhibited the shortest diradical lifetimes.

3.6 Product energy partitioning

We computed the energies of the product fragments from post-TS trajectories initiated from various transition states during the dissociation process. During the formation of the products **Cp** and N_2, the total kinetic energy available to the system is redistributed among the translational, rotational, and vibrational degrees of freedom of the products. Investigating the internal energies of the formed products is therefore of interest. The products were identified by monitoring the two C–N bonds during the course of the trajectory. The products were considered formed if the two C–N bond lengths reached 15 Å and the C(1)–C(3) bond was formed, resulting in ring closure. The internal energies of the N_2 and **Cp** groups were calculated as described elsewhere.[52]

The average relative translational energies ($\bar{E}_{trans}$), rotational energies of **Cp** ($\bar{E}_{rot}$ (**Cp**)), and rotational energies of N_2 ($\bar{E}_{rot}$ (N_2)) were determined for trajectories integrated from the synchronous transition state (**TS1**), the asynchronous transition states (**TS3a**, **TS3c**, **TS4a**, **TS4c**, **TS5**), and the **SOS** region. The results are shown in Fig. 9.

As depicted in Fig. 9(a), the $\bar{E}_{trans}$ between the **Cp** and N_2 fragments initially increases with d_S during the C–N bond-breaking process, eventually plateauing at ∼5 Å for all trajectories integrated from different transition state regions (**TS1**, **TS3a**, **TS3c**, **TS4a**, **TS4c**, **TS5**) and the **SOS** region. However, due to differences in the pathways followed by synchronous (**TS1**, **SOS**) and asynchronous (**TS3a**, **TS3c**, **TS4a**, **TS4c**, **TS5**) trajectories, variations in post-TS/SOS kinetic energy release are observed.

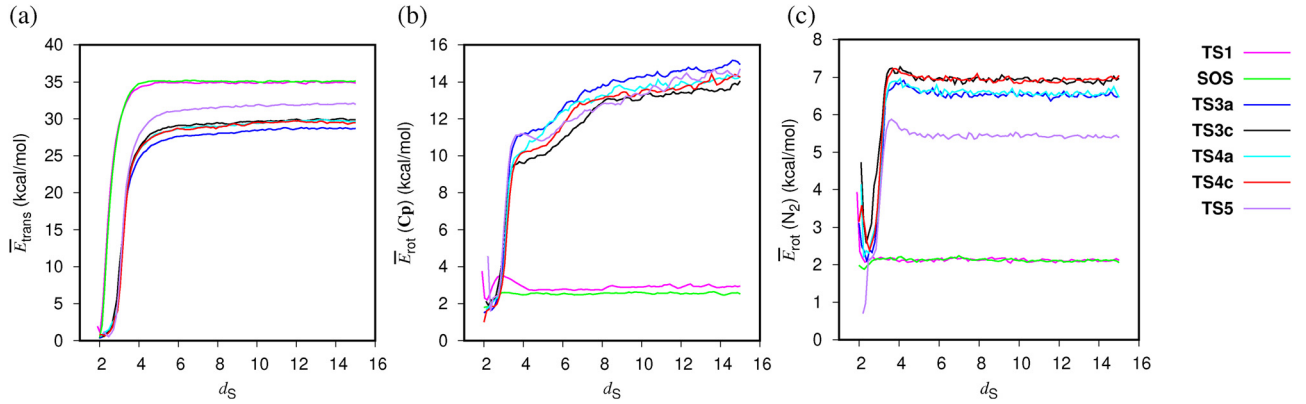

Fig. 9 Plots of average (a) relative translational energies (kcal mol^{-1}), (b) rotational energies of **Cp**, and (c) rotational energies of N_2 as a function of the mean C–N distance d_S (Å) for trajectories integrated from the **TS1**, **SOS**, **TS3a**, **TS3c**, **TS4a**, **TS4c**, and **TS5** regions.

Trajectories from **TS1** and **SOS** regions exhibit higher $\bar{E}_{trans}$ because they involve synchronous breaking of both C–N bonds and immediate formation of the C1–C3 bond. This is accompanied by lower $\bar{E}_{rot}$ for both N_2 and **Cp**, as shown in Fig. 9(b) and (c). Notably, $\bar{E}_{trans}$ is slightly higher for **SOS** trajectories compared to **TS1** trajectories, as the former involves direct formation of **Cp** rather than the intermediate **Int1** seen in the latter.

In contrast, trajectories from asynchronous transition states exhibit lower $\bar{E}_{trans}$ due to the involvement of **TMD** and **DZ** intermediates, which facilitate energy redistribution among the internal degrees of freedom. Among these, **TS5** trajectories exhibit relatively higher $\bar{E}_{trans}$ because, in most cases, the C3–N4 bond dissociates directly from the transition state region, forming SI **Cp** in approximately 65 fs. This is consistent with the lower average rotational energy of the N_2 fragment observed in **TS5** trajectories compared to those initiated from other asynchronous stepwise transition states (**TS3a**, **TS3c**, **TS4a**, **TS4c**).

For trajectories following asynchronous stepwise pathways, the N_2 group rotates around the C3–N4 bond to access different asynchronous intermediates before breaking the C3–N4 bond to form **Cp**. This results in higher $\bar{E}_{rot}$ for both **Cp** and N_2, as shown in Fig. 9(b) and (c).

4 Summary and conclusions

The post-transition state and post-second-order saddle dynamics of the thermal denitrogenation of 1-pyrazoline were investigated using *ab initio* classical trajectory simulations. Trajectories were initiated from different transition state regions corresponding to synchronous and asynchronous pathways, which involve simultaneous and sequential breaking of the two C–N bonds, respectively.

Trajectories initiated from the synchronous transition state (**TS1**) region predominantly followed the minimum energy pathway, leading to the formation of the trimethylene diradical (**Int1**). This intermediate subsequently formed cyclopropane (**Cp**) with a preference for single inversion of the configuration. In contrast, most of the trajectories integrated from the **SOS** region exhibited no inversion at the terminal C1 and C3 carbon centers of **Int1**, resulting in **Cp** with retention of the configuration.

For trajectories initiated from the asynchronous transition state regions, most did not follow the minimum energy pathway (MEP). Although these trajectories accessed both the diazenyl diradical and trimethylene diradical regions, the average lifetimes of the diazenyl diradical were longer than those of the trimethylene diradical. The majority of the trajectories initiated from the **TS5** region followed the minimum energy path corresponding to a concerted N_2 extrusion *via* an S_H2 pathway and resulted in significant inversion at the C3 carbon bonded to the N_2 group in the transition state.

During the dissociation process, all trajectories passed through the diradical region, regardless of the pathway followed. The **TS1** and **SOS** trajectories, which follow the synchronous path, exhibited shorter trimethylene diradical lifetimes, averaging 128 fs and 100 fs, respectively. In contrast, asynchronous trajectories initiated from the **TS3a**, **TS3c**, **TS4a**, and **TS4c** regions displayed longer diradical (**DZ**+**TMD**) lifetimes, with averages of 206 fs, 192 fs, 199 fs, and 178 fs, respectively. However, the trimethylene diradical in these asynchronous pathways remained short-lived, with average lifetimes of 55 fs, 55 fs, 46 fs, and 54 fs, respectively. Interestingly, the average diradical (**DZ**+**TMD**) lifetime for **TS5** trajectories following the S_H2 pathway was the shortest ($\sim$65 fs). The non-exponential distribution of diradical lifetimes observed in trajectories initiated from different transition-state regions possibly indicates incomplete intramolecular vibrational energy redistribution, leading to a nonstatistical product distribution.[53,54]

In the simulations, the SI products ranged from 50% to 65.6% for 1-pyrazoline, depending on the pathway followed, compared to 73% observed in the experiments for *trans*-3,5-dimethyl-1-pyrazoline.[16] When weighted by the expected incidence corresponding to the channels, the product distributions for the SI, DI, and retention products become 52.2%, 35.9%, and 11.8%, respectively. The discrepancies in the product distributions can be attributed to the effect of the methyl substituent, which is not considered in the present study.

In the literature, various intuitive synchronous pathways[16,18] as well as asynchronous pathways backed by CI calculations[26,27]

have been proposed to account for the major SI Cp product observed experimentally in the thermal denitrogenation of 1-pyrazoline. Interestingly, our trajectory simulations reveal that the preference for SI **Cp** formation is independent of the reaction pathway. Both synchronous and asynchronous pathways yield similar stereochemical distributions of products, with trajectories from all six transition state regions showing a preference for SI **Cp** formation. Despite the significant lifetimes of diradical intermediates, the observed preference for SI **Cp** formation underscores the importance of dynamical effects in product formation and suggests the possibility of dynamical matching, as described by Carpenter.[55]

Data availability

The data supporting this article are available from the corresponding author upon reasonable request.

Conflicts of interest

There are no conflicts to declare.

Acknowledgements

The authors thank NISER Bhubaneswar for the computational facilities.

References

1 H.-U. Reissig and R. Zimmer, *Chem. Rev.*, 2003, **103**, 1151–1196.
2 C. A. Carson and M. A. Kerr, *Chem. Soc. Rev.*, 2009, **38**, 3051–3060.
3 P. Tang and Y. Qin, *Synth.*, 2012, **44**, 2969–2984.
4 D. Y.-K. Chen, R. H. Pouwer and J.-A. Richard, *Chem. Soc. Rev.*, 2012, **41**, 4631–4642.
5 R. D. Taylor, M. MacCoss and A. D. Lawson, *J. Med. Chem.*, 2014, **57**, 5845–5859.
6 T. T. Talele, *J. Med. Chem.*, 2016, **59**, 8712–8756.
7 J. Shearer, J. L. Castro, A. D. Lawson, M. MacCoss and R. D. Taylor, *J. Med. Chem.*, 2022, **65**, 8699–8712.
8 R. G. Bergman, *J. Am. Chem. Soc.*, 1969, **91**, 7405–7411.
9 R. Faust, *Angew. Chem., Int. Ed.*, 2001, **40**, 2251–2253.
10 H. Lebel, J.-F. Marcoux, C. Molinaro and A. B. Charette, *Chem. Rev.*, 2003, **103**, 977–1050.
11 C. Ebner and E. M. Carreira, *Chem. Rev.*, 2017, **117**, 11651–11679.
12 L. Dian and I. Marek, *Chem. Rev.*, 2018, **118**, 8415–8434.
13 D. E. Lewis, *Angew. Chem., Int. Ed.*, 2013, **52**, 11704–11712.
14 K. L. Rinehart Jr and T. V. Van Auken, *J. Am. Chem. Soc.*, 1960, **82**, 5251.
15 P. S. Engel, *Chem. Rev.*, 1980, **80**, 99–150.
16 R. J. Crawford and A. Mishra, *J. Am. Chem. Soc.*, 1966, **88**, 3963–3969.
17 H. Meier and K.-P. Zeller, *Angew. Chem., Int. Ed. Engl.*, 1977, **16**, 835–851.
18 T. C. Clarke, L. A. Wendling and R. G. Bergman, *J. Am. Chem. Soc.*, 1977, **99**, 2740–2750.
19 E. Muray, O. Illa, J. A. Castillo, Á. Álvarez-Larena, J. L. Bourdelande, V. Branchadell and R. M. Ortuño, *J. Org. Chem.*, 2003, **68**, 4906–4911.
20 M. Hamaguchi, M. Nakaishi, T. Nagai and H. Tamura, *J. Org. Chem.*, 2003, **68**, 9711–9722.
21 J. L. Garcia Ruano, S. A. Alonso de Diego, M. R. Martn, E. Torrente and A. M. Martin Castro, *Org. Lett.*, 2004, **6**, 4945–4948.
22 J. L. Garcia Ruano, M. T. Peromingo, M. R. Martn and A. Tito, *Org. Lett.*, 2006, **8**, 3295–3298.
23 D. Cruz Cruz, F. Yuste, M. R. Martin, A. Tito and J. L. Garcia Ruano, *J. Org. Chem.*, 2009, **74**, 3820–3826.
24 S. Shiraki, C. S. Vogelsberg and M. A. Garcia-Garibay, *Photochem. Photobiol. Sci.*, 2012, **11**, 1929–1937.
25 T. Y. Chang, D. M. Adrion, A. R. Meyer, S. A. Lopez and M. A. Garcia-Garibay, *J. Org. Chem.*, 2022, **87**, 2277–2288.
26 P. B. Condit and R. G. Bergman, *J. Chem. Soc., Chem. Commun.*, 1971, 4b-6.
27 P. C. Hiberty and Y. Jean, *J. Am. Chem. Soc.*, 1979, **101**, 2538–2543.
28 P. Cadman, H. Meunier and A. Trotman-Dickenson, *J. Am. Chem. Soc.*, 1969, **91**, 7640–7644.
29 G. Loper and F. Dorer, *J. Am. Chem. Soc.*, 1973, **95**, 20–27.
30 P. Mahata, A. K. Rauta and B. Maiti, *J. Chem. Phys.*, 2022, **157**, 194302.
31 J. Jiménez, J. Bourdelande and R. M. Ortuño, *Tetrahedron*, 1997, **53**, 3777–3786.
32 M. Hamaguchi, M. Nakaishi, T. Nagai, T. Nakamura and M. Abe, *J. Am. Chem. Soc.*, 2007, **129**, 12981–12988.
33 W. L. Carter and R. G. Bergman, *J. Am. Chem. Soc.*, 1968, **90**, 7344–7346.
34 R. G. Bergman and W. L. Carter, *J. Am. Chem. Soc.*, 1969, **91**, 7411–7425.
35 J. A. Berson and J. M. Balquist, *J. Am. Chem. Soc.*, 1968, **90**, 7343–7344.
36 R. Pradhan and U. Lourderaj, *Phys. Chem. Chem. Phys.*, 2017, **19**, 27468–27477.
37 C. Doubleday, K. Bolton and W. L. Hase, *J. Am. Chem. Soc.*, 1997, **119**, 5251–5252.
38 C. Doubleday, K. Bolton and W. L. Hase, *J. Phys. Chem. A*, 1998, **102**, 3648–3658.
39 D. J. Mann and W. L. Hase, *J. Am. Chem. Soc.*, 2002, **124**, 3208–3209.
40 R. Pradhan and U. Lourderaj, *Phys. Chem. Chem. Phys.*, 2019, **21**, 12837–12842.
41 B. O. Roos, *Adv. Chem. Phys.*, 1987, 399–445.
42 W. Hehre, L. Radom, P. v. R. Schleyer and J. A. Pople, *Ab Initio Molecular Orbital Theory*, J. Wiley and Sons, New York, 1986.
43 T. H. Dunning Jr, *J. Chem. Phys.*, 1989, **90**, 1007–1023.
44 R. A. Kendall, T. H. Dunning Jr and R. J. Harrison, *J. Chem. Phys.*, 1992, **96**, 6796–6806.
45 P. Ren, C. Wu and J. W. Ponder, *J. Chem. Theory Comput.*, 2011, **7**, 3143–3161.
46 W. L. Hase, *Classical trajectory simulations: Initial conditions*, Wiley Online Library, 2002, vol. 1, pp. 402–407.

47 K. Yadav, R. Pradhan and U. Lourderaj, *Faraday Discuss.*, 2022, **238**, 183–203.
48 U. Lourderaj, R. Sun, S. C. Kohale, G. L. Barnes, W. A. de Jong, T. L. Windus and W. L. Hase, *Comput. Phys. Commun.*, 2014, **185**, 1074–1080.
49 M. Valiev, E. Bylaska, N. Govind, K. Kowalski, T. Straatsma, H. V. Dam, D. Wang, J. Nieplocha, E. Apra, T. Windus and W. de Jong, *Comput. Phys. Commun.*, 2010, **181**, 1477–1489.
50 S. Pedersen, J. Herek and A. Zewail, *Sci.*, 1994, **266**, 1359–1364.
51 A. Sinicropi, C. S. Page, W. Adam and M. Olivucci, *J. Am. Chem. Soc.*, 2003, **125**, 10947–10959.
52 W. L. Hase, *Encyclopedia of Computational Chemistry*, 2002, vol. 1, pp. 399–402.
53 U. Lourderaj and W. L. Hase, *J. Phys. Chem. A*, 2009, **113**, 2236–2253.
54 B. Jayee and W. L. Hase, *Annu. Rev. Phys. Chem.*, 2020, **71**, 289–313.
55 B. K. Carpenter, *J. Am. Chem. Soc.*, 1985, **107**, 5730–5732.